High-Resolution Infrared Spectroscopy of HCN−Ag_n ($n = 1-4$) Complexes Solvated in Superfluid Helium Droplets†

Paul L. Stiles* and Roger E. Miller‡

Department of Chemistry, University of North Carolina, Chapel Hill, North Carolina 27599

Received: January 30, 2007; In Final Form: April 12, 2007

High-resolution infrared spectroscopy has been used to determine the structures, C−H stretching frequencies, and dipole moments of the HCN−Ag_n ($n = 1-3$) complexes formed in superfluid helium droplets. The HCN−Ag_4 cluster was tentatively assigned based upon pick-up cell pressure dependencies and harmonic vibrational shift calculations. Ab initio and density functional theory calculations were used in conjunction with the high-resolution spectra to analyze the bonding nature of each cluster. All monoligated species reported here are bound through the nitrogen end of the HCN molecule. The HCN−Ag_n complexes are structurally similar to the previously reported HCN−Cu_n clusters, with the exception of the HCN−Ag binary complex. Although the interaction between the HCN and the Ag_n clusters follows the same trends as the HCN−Cu_n clusters, the more diffuse nature of the electrons surrounding the silver atoms results in a much weaker interaction.

I. Introduction

The study of metal clusters and their interactions with molecules has greatly increased our understanding of the nanoscale world.[1−6] Through experiment and theory, it has been well-established that the properties of metal clusters can vary dramatically with just the addition or subtraction of a single metal atom.[7,8] The molecular nature of metal clusters has inspired further investigation with the hope of designing clusters that preferentially catalyze one reaction over another, providing potentially powerful tools to the synthetic, materials, and nanoscience communities. The beneficiaries of these studies are not limited to the field of heterogeneous catalysis. There is intense interest in the design and application of molecular electronic devices.[9,10] Unfortunately, the lack of detailed knowledge of the interactions that take place between molecules and molecular contacts, often represented by small metal clusters, has stymied progress in this area.[9]

Over the years, some of the techniques used to probe the fundamental properties of both bare and ligated metal clusters include mass spectrometry,[11,12] electronic spectroscopy,[13] and, to a lesser extent, microwave[14] and infrared (IR) spectroscopies.[5,15,16] In the study of interactions between adsorbates and metal clusters, few techniques offer more information than IR spectroscopy. Unfortunately, although IR data exist for molecule−metal ion systems[5,6] and a limited number of ligated neutral metal clusters,[17,18] rotationally resolved IR data for adsorbates bound to neutral metal clusters is generally lacking.

It is the sincere goal of this laboratory to convince the general metal cluster field of the great potential that superfluid helium droplets have in the study of metal clusters. Superfluid helium droplets have proven to be a nearly ideal spectroscopic matrix and have been applied to the study of several very different systems.[19−24] The technique is particularly well-suited to the study of metal cluster−adsorbate systems. For one, the pick-up technique allows for the controlled growth of metal cluster sizes ranging from small (2−6 atoms) to very large (>100 atoms).[25,26] Also, the virtually perturbation-free ultracold environment of the helium droplet allows for the acquisition of rotationally resolved IR spectra, thus revealing the structures of the solvated complexes, a rare and valuable piece of experimental information.

In a recent publication,[27] we reported the high-resolution IR spectra of three monoligated copper clusters, namely, HCN−Cu_n ($n = 1-3$), that were formed and probed within superfluid helium droplets. Through the symmetry of the rotationally resolved spectra, we were able to assign the structure to each complex. The interaction between the HCN and the copper clusters varied greatly with cluster size and, in the case of HCN−Cu_2 and HCN−Cu_3, were much stronger than the interaction between HCN and bulk copper. Contrary to what we have seen in previous, albeit more weakly bound, systems was that the most weakly bound complex (HCN−Cu) had a C−H vibrational frequency that was shifted furthest to the red while the corresponding band in the most strongly bound complex (HCN−Cu_3) was red-shifted the least. From our previous experience with weakly bound complexes, we expected the exact opposite to be true and concluded that the observed inverse relationship between red shift and binding energy was due to a fundamental change in the nature of the bond between HCN and the copper clusters.[22,27−29] We visualized the changes in bonding through the use of electron density difference plots that showed a clear buildup of electron density between the HCN and the Cu_n as the cluster grew in size. This increased bonding was determined to be consistent with the nature of bonding previously determined by Fournier in the CO−Cu_n ($n = 1-3$) clusters.[30] As a follow up to the previous work, we progress down the coinage metal column of the periodic table and report the IR spectra of HCN bonded to small silver clusters ($n = 1-4$).

† Part of the "Roger E. Miller Memorial Issue".

* To whom correspondence should be addressed. E-mail: pstiles@northwestern.edu. Current address: Department of Chemistry, Northwestern University, Evanston, Illinois 60208.

‡ Deceased: November 6, 2005.

10.1021/jp0707945 CCC: $37.00
Published on Web 05/23/2007

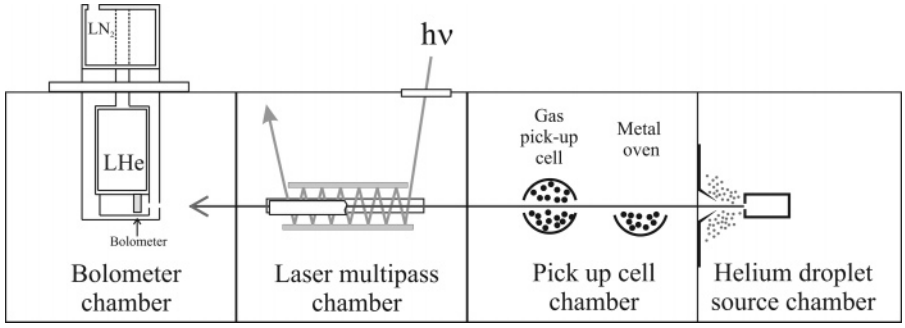

Figure 1. Schematic of the differentially pumped helium droplet spectroscopy instrument. The droplets are formed in the source chamber and skimmed before entering the pick-up cell chamber where the doping of the droplets takes place. The helium droplet beam then enters the laser multipass chamber where the IR photons interact with the clusters embedded in the droplets. The beam is detected by a liquid helium-cooled bolometer in the final chamber.

II. Experimental Section

Figure 1 shows a schematic of our latest helium droplet instrument.[31] Much of our work over the last 2 years has been accomplished with this instrument, and it is useful to describe several of its features. The biggest difference between this apparatus and the one described previously[32,33] is the breakup of the source, pick-up, laser interaction, and bolometer sections into four separate chambers. All of the chambers are differentially pumped and connected to each other through a small 0.5″ gate−valve opening. The gate valves allow individual chambers to be vented, while the remaining chambers are left under vacuum.

The droplets were formed by expanding ultrapure helium through a 5 μm nozzle. The nozzle was cooled, using a closed-cycle helium refrigerator, to temperatures in the range of 19 to 16 K, backed with 60 bar of helium pressure, corresponding to average droplet sizes of approximately 6000−12000 helium atoms, respectively.[34] After droplet formation and skimming, the droplet beam was passed just over the top of a resistively heated alumina crucible, which contains the silver shot. The droplets then pass through a differentially pumped HCN gas pick-up cell, where the final complexes are formed.

An F-center laser (Burleigh FCL-20), operating on crystal #3 (RbCl:Li), was brought into the chamber through a CaF_2 window. The beam was reflected between two gold mirrors oriented on either side of the helium droplet beam. The various HCN−Ag_n ($n = 1-4$) clusters were excited by tuning the laser into resonance with their corresponding C−H stretching frequencies. Subsequent vibrational relaxation to the helium droplet resulted in the evaporation of approximately 600 helium atoms per doped droplet, if it assumed that each doped droplet encounters only one photon and that one helium atom is evaporated per 5 cm^{-1} of energy.[35] This approximation is sound, given the lower laser power associated with the F-center laser (∼5 mW). The amplitude-modulated laser-induced beam depletion was monitored using a liquid heluim-cooled bolometer (Infrared Laboratories) and a lock-in amplifier (Stanford Research Systems SR510). The details associated with tuning and calibrating the laser can be found elsewhere.[36]

An electric field could be applied to the laser interaction region using two metal electrodes shown in the laser multipass chamber in Figure 1 (the near electrode in the figure is cut away). A considerable enhancement of the signal levels was obtained by using a large electric field (∼24 kV/cm) to record pendular spectra,[37,38] which was particularly useful when searching for new species. At more modest electric fields[39] (1−4 kV/cm), the resulting Stark spectra provided an accurate measure of the dipole moments of the HCN−Ag_n complexes.[40]

TABLE 1: Bond Length (R_e) and Harmonic Frequency (ω_e) of the $^1\Sigma_g^+$ Ground State of Ag_2 as Compared with Previous Work

Ag_2	R_e (Å)	ω_e (cm^{-1})
RMP2	2.5812	177.56
B3LYP	2.5888	178.11
B3LYP[a]	2.611	177.1
Expt[b]	2.530	192

[a] Ref 47. [b] Ref 46.

TABLE 2: $^2B_2$ Electronic State of Ag_3 Is a Jahn−Teller Distorted Obtuse Triangle[a]

Ag_3	R_e	θ	$\omega_{S.S.}$	$\omega_{A.S.}$	ω_{bend}
ROMP2	2.6479	68.12°	167.8	104.8	62.7
CCSD(T)[b]	2.695	67.88°	166.4		57.8

[a] The bond length of legs (R_e) and bond angle (θ) of the triangle are given, along with the symmetric stretch ($\omega_{S.S.}$), asymmetric stretch ($\omega_{A.S.}$), and bending (ω_{bend}) harmonic frequencies. Previous CCSD(T) results are also given for comparison purposes. Bond lengths are given in Angstroms, and frequencies are given in cm^{-1}. [b] Ref 48.

In our previous helium droplet machine, the bolometer was housed within the chamber that also contained the pick-up cells and metal ovens. While this setup was adequate for the measurement of volatile gases, complications arose upon the introduction of relatively large amounts of metal vapor to the chamber. A period of 2 or 3 days of experiments gave way to significant reductions in bolometer sensitivity as the diamond collector on the bolometer became coated with the metal under investigation. The new instrument (Figure 1) has the bolometer chamber separated from the pick-up cell chamber, which has eliminated the problem of bolometer coating.

A. Computational Details. The MP2 calculations were performed using Molpro.[41] All DFT calculations were performed with Gaussian 03.[42] In all calculations, we used the small core Stuttgart−Dresden effective core potential (ECP) (ECP28mhf)[43] along with the Stuttgart−Dresden valence basis set for Ag (8s,7p,6d) → [6s,5p,3d], which was augmented with 2f functions and a 1g function, as optimized by Martin and Sundermann.[44] The 6-311++G(d,p) basis set was used for HCN.

Because of their similar electronic structures, it was anticipated that the HCN−Ag_n system would exhibit many of the characteristics found in the HCN−Cu_n complexes. As a result, we repeated the methods used in the HCN−Cu_n complexes by using restricted open-shell (RO)MP2 methods as opposed to unrestricted (U)MP2 for the open-shell HCN−Ag and HCN−Ag_3 complexes. We also performed DFT calculations using the same ECPs and basis sets, using the B3LYP functional. The interpretation of the results required some caution due to the poor performance of DFT with weakly bound complexes.[45] The

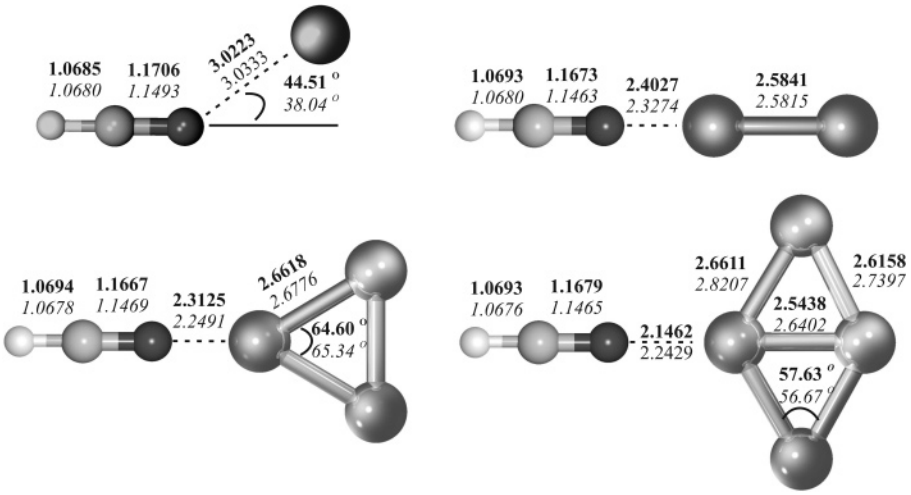

Figure 2. Structures of the HCN−Ag_n ($n = 1-4$) complexes. The MP2 bond lengths and angles are given in the upper set of numbers (bold), while the B3LYP bond lengths and angles are given as the lower set (in italics). For comparison, the calculated MP2 bond lengths for C−H and C−N in HCN are 1.0680 and 1.1713 Å, respectively. The DFT bond lengths are 1.0668 and 1.1491 Å.

results of our calculations are given in Tables 1 and 2 and Figure 2. Comparisons of our silver cluster results to previous experimental[46] and theoretical[47,48] work show excellent agreement in all cases.

There is currently no previous work on which to directly compare our HCN−Ag_n calculations; however, there does exist some recent work regarding the CO−Ag_n complexes.[49,50] HCN and CO are isoelectronic and have very similar molecular orbitals, and consequently, we expect to find many similar binding patterns between the Ag_n clusters and the two ligands. Indeed, the reported structures for the HCN−Cu_n complexes were very similar to the available Cu_n−CO structures.[27] A quick comparison between the structures shown in Figure 2 with the Ag_n−CO structures reported by Joshi et al.[50] and Zhou et al.[49] shows some slight differences, namely, the structures of the Ag_2−CO and HCN−Ag_2 complexes. Both Zhou and Joshi report bent structures for the Ag_2−CO, while we report a linear HCN−Ag_2 structure. To investigate this further, we repeated our methods on the Ag_2−CO complex. Using MP2 methods produced a linear structure, while the B3LYP method reproduced the bent structure reported by the other groups. A very similar discrepancy was found in the Cu_2−CO complex, where one group reported a linear structure, while another claimed that Cu_2−CO was bent.[51] It was concluded by Poater et al. that the potential energy surface connecting the two structures was extremely flat and any slight difference in basis set and/or level of theory could favor one structure over another.

III. Results

A. Pendular Spectrum. The method of pendular spectroscopy[53] has been shown to be extremely useful in the search of new, previously unobserved, vibrational bands. As discussed above, a large electric field (~24 kV/cm), parallel to the $\vec{E}$ field of the linear polarized F-center laser, was applied to the laser interaction region of the experimental apparatus. In the case of a parallel band, the field orients the vibrational transition moment along with the laser polarization and collapses the rotational structure, thus giving a large increase in signal-to-noise. The pendular spectrum of HCN−Ag_n ($n = 1-3$) is shown in Figure 3 and was acquired with an average droplet size of 5700 He atoms, a HCN pressure of 2.0×10^{-6} Torr, and a helium backing pressure of 60 bar. The well-known HCN and HCN dimer pendular bands are labeled along with HCN−Ag_n

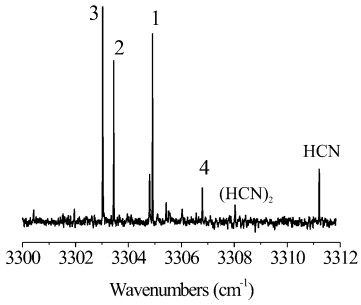

Figure 3. Pendular spectrum covering the free C−H stretch region of the HCN−Ag_n ($n = 1-4$) clusters. The monoligated silver cluster sizes are labeled in the figure. This spectrum was taken with very low HCN pressures (2×10^{-6} Torr) to minimize the signal contributions of HCN multimer peaks.

assignments,[32] which were determined through a combination of using signal dependence techniques, field free spectra, and dipole moment measurements.

Let us begin with the determination of the peak assignments using signal optimization techniques. We began our search for the HCN−Ag_n complexes by fixing the laser frequency to the pendular transition of HCN monomer (3311.21 cm^{-1}) and slowly heating the silver-filled crucible. As the vapor pressure of the silver increased and began to dope the helium droplets, the total number of droplets containing a single HCN molecule went down, which was reflected in the decreasing HCN pendular signal. We continued heating the silver until the HCN signal was depleted by about 30%, at which point our search for new peaks in the spectrum began. The first new peak grew in at about 3305 cm^{-1} and has since been assigned to the nitrogen-bonded HCN−Ag binary complex.

During a typical experiment, when a new peak is discovered, the laser is tuned to the peak of an individual pendular band. The HCN pressure, average droplet size, and metal oven temperature are then adjusted until the optimal signal is attained. Because the pick-up of dopants by helium droplets is known to occur via Poisson statistics,[35] adjusting these variables gives a good idea of which complexes correspond to which bands. Consider, for example, the band at 3304.9 cm^{-1}. At oven temperatures below 830 °C (10^{-4} Torr vapor pressure of Ag), it is the only peak present besides the HCN multimer peaks. Tuning the laser frequency to the pendular band at 3304.9 cm^{-1} and adjusting the HCN pick-up cell pressure to maximize the

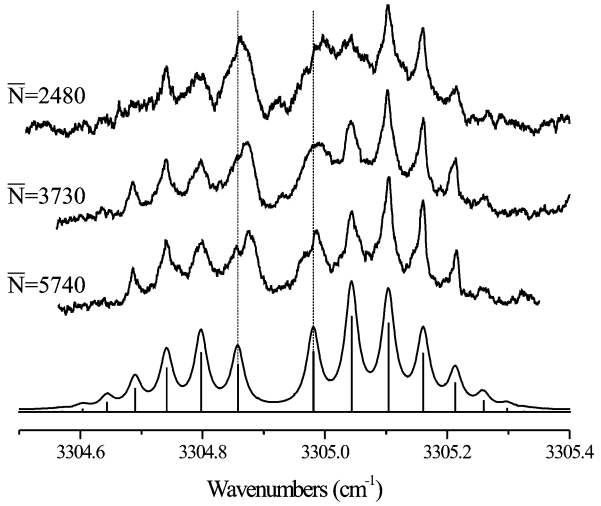

Figure 4. Three field free spectra of HCN−Ag taken at three different average droplet sizes. The lowest spectrum was simulated by fitting the P(2)−P(4) and R(1)−R(4) rovibrational bands to a linear rotor Hamiltonian. The rotational temperature was fixed to 0.37 K, and a line width of 0.025 cm^{-1} (fwhm) was used. A stick spectrum is also given to guide the eye and illustrate why we disregarded the P(1) and R(0) bands in the fit.

TABLE 3: Vibrational Origin (ν_0, cm^{-1}) and Red Shift ($\Delta\nu_0$, cm^{-1}), from HCN, of the C−H Stretch in HCN−Ag Determined from Experiment and Calculated through ROMP2 and DFT Methods[a]

HCN−Ag				
	expt		ROMP2	B3LYP
ν_0	3304.92			
$\Delta\nu_0$	6.29	$\Delta\nu_0$	5.60	4.70
B''	0.0308	B_e	0.0622	0.0609
B'	0.0313	B_{gas}/B_{He}	2.02	1.98
$\bar{D}$	4.6×10^{-5}			
μ''	4.65 ± 0.05	μ	4.959	3.899
μ'	4.55 ± 0.05			

[a] The experimental linear rotor Hamiltonian rotational constants and dipole moment (μ, Debye) are given in the ground ($''$) and vibrationally excited states ($'$). The distortion constant ($\bar{D}$, cm^{-1}) is given as the average between the ground and the excited states. The theoretical equilibrium rotational constants and dipole moments are given for comparison as well as the ratio between the "gas-phase" rotational constant and the ground state rotational constant measured in helium (B_{gas}/B_{He}).

signal, it was found that the peak's intensity optimized at HCN pressures very near the pressure found to optimize for HCN monomer, namely, 6×10^{-6} Torr, thus giving compelling evidence that the band corresponds to a complex containing a single HCN molecule. Working our way through the other bands, and keeping the HCN pressure relatively low, we found that the peaks assigned to higher order silver clusters required increasingly higher oven temperatures and average droplet sizes. Higher silver temperatures correspond to higher silver vapor pressures and thus a higher probability of multiple collisions between silver atoms and a given helium droplet. The larger HCN−Ag$_n$ clusters optimized with larger droplet sizes for two reasons. One, the larger droplets have greater pick-up cross-sections, and two, they have a greater heat capacity for the dissipation of condensation energy upon silver cluster formation, as discussed in the previous HCN−Cu$_n$ ($n = 1-3$) publication.[27]

B. HCN−Ag. The assignment of each peak is not based solely on the optimization techniques discussed above. The great power of superfluid helium droplet spectroscopy is that rotational resolution is observed in their spectra for species solvated within the droplet. Although the rotational constants are perturbed from their gas-phase counterparts, the overall symmetry of the spectra remains unchanged. The pendular band already assigned to HCN−Ag, based upon optimization techniques, was scanned again in the absence of an electric field. The resulting spectra, taken at three different droplet sizes, are shown in Figure 4. The spectra are that of a linear rotor, which is in agreement with the theoretical structure given in Figure 2. We show the spectra of HCN−Ag at different average droplet sizes because of the anomalous features near the vibrational origin of the spectrum. It appears that there are extra transitions beneath the R(0) and P(1) bands, which become more intense with decreasing average droplet size. The size dependence of the line widths seems to point to droplet size-dependent inhomogeneous broadening mechanisms, which are typically reduced for the larger average droplet sizes.[54−56]

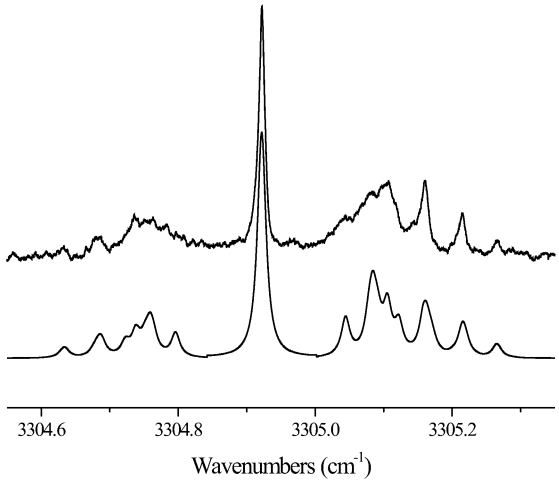

Figure 5. Stark spectrum of HCN−Ag taken at a field of 2.055 kV/cm. The simulated spectrum, given below the experimental spectrum, was generated using our pendular rotor program. See the text for details.

The fitting of the spectrum of HCN−Ag solvated within helium droplets was complicated by the aforementioned anomalous features near the vibrational origin. The rotational constants (B and D) were fit in the ground and vibrationally excited states while ignoring the R(0) and P(1) rovibrational bands. The resulting fit using a line width (fwhm) of 0.025 cm^{-1} is shown in Figure 4, while the resulting rotational constants are given in Table 3. The B rotational constant is reduced from the ROMP2 rotational constant by a factor of 2. As it has been discussed previously, the rotational constants of rotors solvated in helium droplets have been found to be reduced by a factor of 2.5 ± 0.5, as compared to their gas-phase values.[57−60] This is due to the attractive potential between the solvent and the solute, which drags some of the helium density along with the dopant. An understanding of this process is an active area of theoretical research, and significant progress has been made, but unfortunately, a computationally feasible method for the calculation of helium's effect is still beyond the state of the art.[57−62] We will refer to the empirically determined factor of 2.5 throughout this paper when comparing rotational constants.

Another advantage of the free rotation of dopants within superfluid helium droplets is the ability to record the Stark spectra of molecules.[40] Figure 5 shows the Stark spectrum of HCN−Ag taken at a field of 2.055 kV/cm. This spectrum is one of three taken at various fields. The Stark spectrum was simulated using our pendular rotor program,[63] which diagonalizes the Stark Hamiltonian using the asymmetric top wavefunctions truncated at $J = 15$, $K = 12$, and $M = 15$. The rotational constants were taken from the previously determined zero-field

spectrum (Table 3). The simulated Stark spectrum was generated by adjusting the ground and vibrationally excited dipole moments. These results are given in Table 3. It is interesting to note that the vibrationally excited dipole moment ($\mu' = 4.55$ D) was found to be smaller than the ground state dipole moment ($\mu'' = 4.65$ D). This decrease in the vibrationally excited dipole moment is counterintuitive given that the excited C−H stretch elongates the C−H bond and therefore should increase the dipole moment. In a possible related phenomenon, it was found that the vibrationally excited B rotational constant was larger than the ground state. Again, this should be the opposite since the C−H bond length should increase upon vibrational excitation and thus lower the rotational constant.

A comparison with theory reveals that the experimental dipole moment is smaller than the theoretical, namely, 4.959 D for ROMP2 and 4.65 D for the experimental. We do not consider the DFT dipole moment due to DFT's poor performance with weakly bound complexes.[45] This discrepancy between experiment and theory is most likely due to the vibrational averaging that takes place on the HCN−Ag potential energy surface. HCN and Ag are weakly bound (ROMP2 $D_e = -0.26$ kcal/mol) and, as such, can have wide amplitude motion with respect to each other. A full exploration of the degree to which vibrational averaging should have on the measured dipole moment requires a two-dimensional potential energy surface and is beyond the scope of this paper.

During the course of the Stark field measurements, very interesting variations in the line widths and intensities of the individual rovibrational peaks in the HCN−Ag spectra were observed. With very small electric fields applied to the HCN−Ag band, the intensity of the broad features near the vibrational origin decreased dramatically. With slightly higher fields (402 V/cm), an increased intensity in the R(1)−R(5) and P(2)−P(5) rovibrational transitions was seen, resulting in a marked increase in the resolution of the rotational fine structure. Figure 4 shows the spectra of three scans for HCN−Ag, one taken in the absence of a field and two taken with very small applied electric fields. With the exception of the electric fields present, all of the spectra were acquired using identical conditions. Also shown is the stick spectrum that was generated using the rotational constants given in Table 3. Notice that the field taken at 154 V/cm is so weak that a Q-branch is not observed, while at the same time there is a dramatic decrease in the broad features near the P(1) and R(0) bands. In the spectrum taken at a field of 402 V/cm, there is a weak Q-branch and a large increase in the intensity of the rovibrational bands. Typically, intensity is gained in the Q-branch at the expense of the P and R branches when a field is applied. We should note that a similar behavior has recently been observed for the complexes of HCN and atoms known to reside on or very near to the droplet surface, namely, the alkali metals[64] and larger alkaline earth metals (calcium and strontium).[65] It is still unclear if these data are related, but it is interesting to note that the coinage metals have an analogous electronic structure to the alkali metals, and it would not be surprising if it was found that silver has a significant probability of residing near the helium droplet's surface.

C. HCN-Ag_2 and HCN−Ag_3. Figure 3 shows two pendular bands red-shifted with respect to the HCN−Ag complex. These bands optimized at higher oven temperatures and larger average droplet sizes, indicating that they were due to complexes containing multiple silver atoms. The confirmations of the structures and identity of each peak were accomplished through the measurement of their zero field spectra. The vibrational origins of the two bands are relatively close, and for convenience, we will present both spectra simultaneously. Figure 7 shows the field free spectra for HCN−Ag_2 (right) and HCN−Ag_3 (left). Both spectra are clearly different with one being due to a linear rotor (HCN−Ag_2) and the other (HCN−Ag_3) being due to a rotor possessing angular momentum about all three axes (the lack of resolved fine structure suggests an asymmetric top). The higher frequency linear rotor spectrum optimizes at oven temperatures above the previously assigned HCN−Ag and at lower temperatures than the asymmetric top spectrum. Looking to the ab initio structures given in Figure 2, HCN−Ag_2 is a linear rotor and is the only possible complex that can give rise to the linear rotor spectrum shown in Figure 7. Likewise, the asymmetric top spectrum shown in Figure 7 can only be due to the HCN−Ag_3 structure shown in Figure 2.

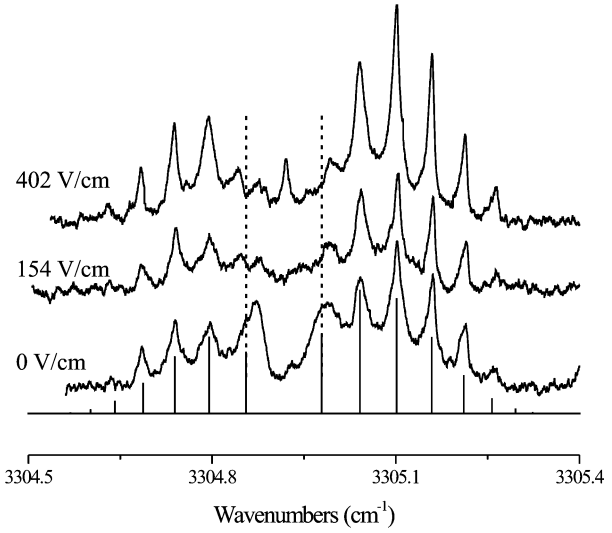

Figure 6. Zero-field and Stark spectra of the HCN−Ag complex. The field strength is given alongside the corresponding spectrum. A stick spectrum using the rotational constants given in Table 3 is also shown. The dotted lines are centered on the P(1) and R(0) bands to guide the eye.

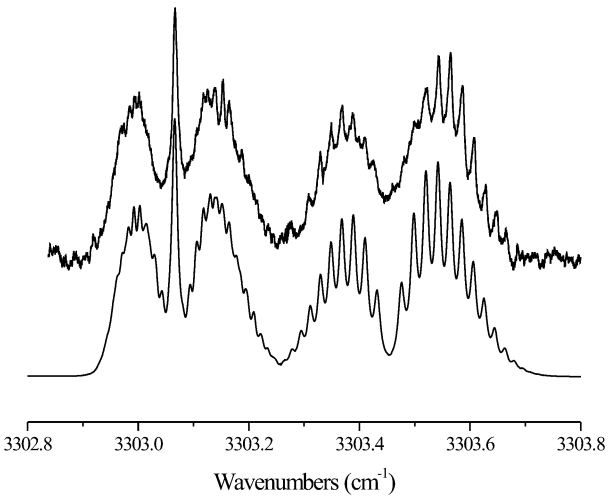

Figure 7. Zero-field spectra of HCN−Ag_2 and HCN−Ag_3. The HCN−Ag_2 was assigned to a linear rotor spectrum (right). The HCN−Ag_3 was assigned to the asymmetric top spectrum (left). The simulated spectra are given below the experimental spectra.

A summary of the theoretically and experimentally determined observables is given in Tables 4 and 5. The rotational constants determined from the fits of each spectrum are consistent with the ab initio structures. The HCN−Ag_2 experimental B rotational constant is reduced by a factor of 1.9 when compared to the calculated ROMP2 and B3LYP rotational

TABLE 4: Vibrational Origin (ν_0, cm^{-1}) and Red Shift ($\Delta\nu_0$, cm^{-1}), from HCN, of the C−H Stretch in HCN−Ag$_2$ Determined from Experiment and Calculated through ROMP2 and DFT Methods[a]

HCN−Ag$_2$				
	expt		MP2	B3LYP
ν_0	3303.45			
$\Delta\nu_0$	7.76	$\Delta\nu_0$	9.73	7.30
$\bar{B}$	0.0110	B_e	0.02068	0.02127
		B_{gas}/B_{He}	1.9	1.9
$\bar{D}$	5.1×10^{-6}			
$\bar{\mu}$	6.8 ± 0.3	μ	6.473	6.542

[a] The experimental linear rotor Hamiltonian rotational constants [$\bar{B}$ (cm^{-1}) and $\bar{D}$ (cm^{-1})] and dipole moments ($\bar{\mu}$, Debye) are given as the average between the ground and the vibrationally excited states. The theoretical equilibrium rotational constants and dipole moments are given for comparison as well as the ratio between the "gas-phase" rotational constant and the ground state rotational constant measured in helium (B_{gas}/B_{He}).

TABLE 5: Vibrational Origin (ν_0, cm^{-1}) and Red Shift ($\Delta\nu_0$, cm^{-1}) from HCN of the C−H Stretch in HCN−Ag$_3$ Determined from Experiment and Calculated through ROMP2 and DFT Methods[a]

HCN−Ag$_3$				
	expt		ROMP2	B3LYP
ν_0	3303.07			
$\Delta\nu_0$	8.14	$\Delta\nu_0$	10.86	8.17
$\bar{A}$	0.03	A_e	0.03862	0.03774
$\bar{B}$	0.00701	B_e	0.01956	0.01999
		B_{gas}/B_{He}	2.8	2.8
$\bar{C}$	0.0055	C_e	0.01299	0.01307
		C_{gas}/C_{He}	2.3	2.3
$\bar{\mu}$	7.5 ± 0.5	μ	6.705	6.763

[a] The experimental asymmetric top Hamiltonian rotational constants [$\bar{A}$, $\bar{B}$, $\bar{C}$ (cm^{-1})] and dipole moments ($\bar{\mu}$, Debye) are given as an average of the ground and vibrationally excited states. The theoretical equilibrium rotational constants and dipole moments are given for comparison.

constants. As for the HCN−Ag$_3$ complex, the experimental A constant is not measurably different from theory, while the B and C constants are reduced by a factor of 2.8 and 2.3, respectively. The C−H stretch in HCN−Ag$_3$ is a parallel band, and as such, it is not possible to precisely measure its A rotational constant. It is possible, however, to arrive at a reliable estimate by adjusting the A constant to match the relative intensity of the Q-branch. It is interesting to note that the B and C constants are reduced by the typical factor of ∼2.5, while there is little reduction in the A rotational constant. This asymmetric nature of helium's effect on each inertial axis has been observed previously.[66,67]

The agreement between the harmonic frequency shifts from HCN monomer is quite good for both the HCN−Ag$_2$ and the HCN−Ag$_3$ complexes, especially for the B3LYP calculations. The MP2 frequency shifts overshoot the experimental values, but the overall trend is reproduced. The dipole moments, on the other hand, (especially the HCN−Ag$_3$ complex) are in fair agreement, at best. The experimental Stark spectra taken at two different fields for these bands are shown in Figure 8 along with the simulated spectra used to determine the dipole moments. It is true that the helium solvent can shield the dopant from the full magnitude of the applied field, but as it was shown previously, this usually affects the measured dipole moment by 1−2%.[40]

D. HCN−Ag$_4$. In Figure 3, we have tentatively assigned the small peak at 3306.8 cm^{-1} to the HCN−Ag$_4$ complex. The structure and bond lengths of the HCN−Ag$_4$ complex, calculated at the MP2 and B3LYP level, are given in Figure 2. Because of computational costs, we only present the B3LYP vibrational frequency calculations. The B3LYP C−H stretch frequency for this complex was calculated to be red-shifted by 5.3 cm^{-1} from the HCN monomer. Interestingly, this red shift is less than the red shift calculated for the HCN−Ag$_3$ complex and is consistent with what was measured and calculated for the HCN−Cu$_n$ system.[27] Notice that the pendular peak in Figure 3, labeled 4, is near the theoretical vibrational shift of HCN−Ag$_4$ (3305.9 cm^{-1}). This band optimized at even higher oven temperatures than the HCN−Ag$_2$ and HCN−Ag$_3$ bands while also optimizing at low HCN pressures, giving strong evidence that it corresponds to the HCN−Ag$_4$ complex. Unfortunately, its intensity was too weak for a rotationally resolved spectrum to be acquired and we cannot definitively assign it to the structure given in Figure 2.

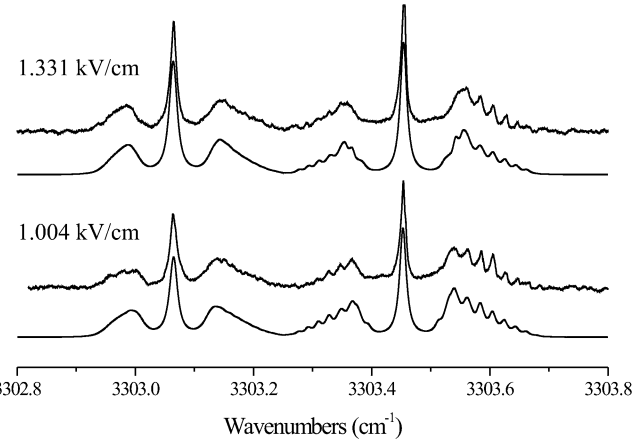

Figure 8. Stark spectra of HCN−Ag$_2$ and HCN−Ag$_3$. The simulated spectra used to determine the dipole moments are shown below the experimental spectra.

IV. Discussion

We will begin the discussion with some direct comparisons of the HCN−Ag complex with the previously reported HCN−Cu species. Such comparisons show several significant differences, with the most obvious being the geometries of the two complexes, revealing an underlining fundamental difference in the binding nature of the two complexes. As it was discussed in the previous publication,[27] the Ag atom is much larger than the Cu atom and has several implications to both the computational and the experimental results of each complex. With regard to the computational results, the geometry of the HCN−Ag complex is bent, with a relatively large N−Ag bond length (3.022 Å) and a very weak binding energy (−0.26 kcal/mol), while the HCN−Cu complex was calculated with a linear geometry, a much smaller N−Cu bond length (1.925 Å), and much larger binding energy (−1.73 kcal/mol). The difference between HCN−Cu and HCN−Ag can be attributed to the diffuse nature of the silver atom, as the Pauli repulsion prevents the nitrogen lone pair from donating charge to the half-filled 5s orbital. The HCN−Ag interaction is more van der Waals in nature than the HCN−Cu interaction. In fact, the bent geometry of HCN−Ag more closely resembles the closed-shell HCN−Mg and HCN−Zn complexes.[29,68] Additionally, the calculated binding energy between the HCN and the Ag is also much closer to the HCN−Mg [D_e (MP2) = −0.51 kcal/mol] and HCN−Zn [D_e (MP2) = −0.34 kcal/mol] complexes than was the HCN−Cu complex (Table 6).

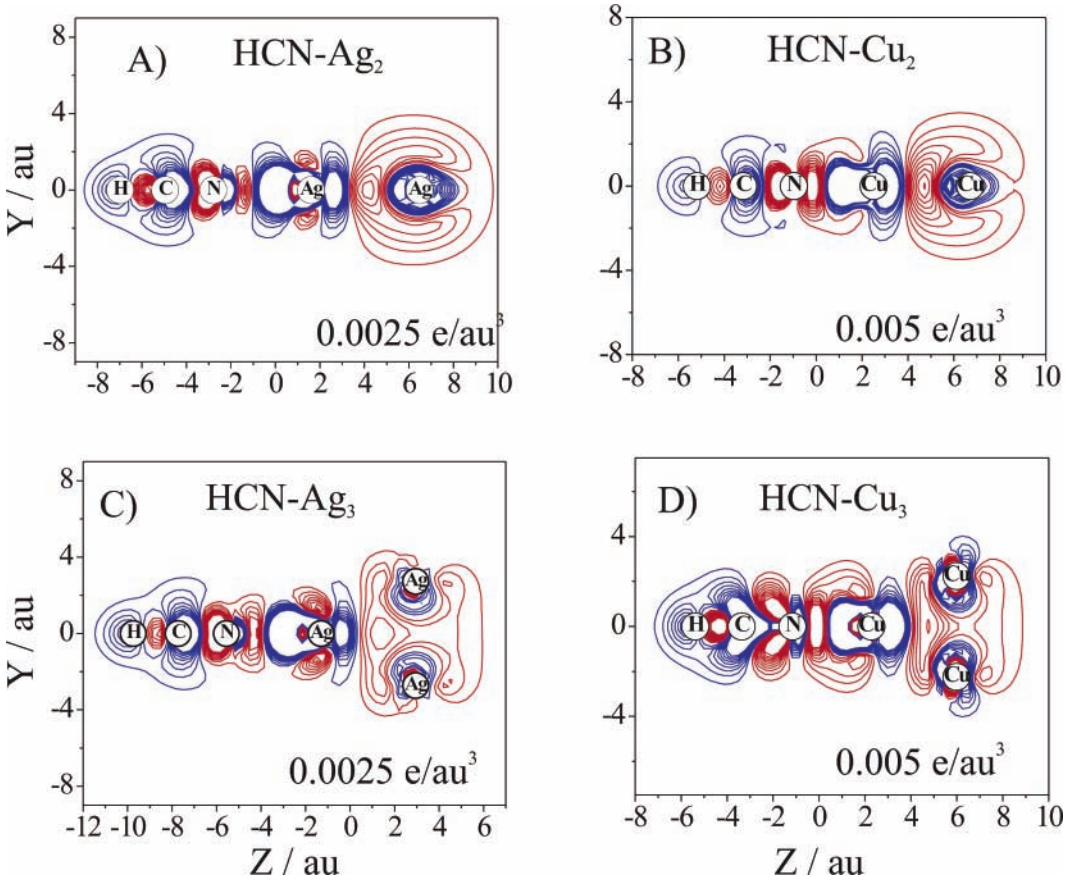

Figure 9. Electron density difference plot of (A) HCN−Ag_2, (B) HCN−Cu_2, (C) HCN−Ag_3, and (D) HCN−Cu_3 calculated at the MP2 level. Contours range from −0.0025 to +0.0025 e/au^3 and are spaced at 0.00025 e/au^3 intervals for plots A and C and range from −0.005 to +0.005 e/au^3 and are spaced at 0.0005 e/au^3 intervals for plots B and D. Positive and negative contours are given in red and blue, respectively. ECP and basis set information can be found in the text.

TABLE 6: Compilation of the MP2 and B3LYP Binding Energies (De) between the HCN Ligand and the Given Coinage Metal Cluster[a]

complex	RMP2	B3LYP
HCN···Cu	−1.73	−2.92
HCN···Ag	−0.258	
HCN···Cu_2	−16.2	−14.4
HCN···Ag_2	−6.25	−6.57
HCN···Cu_3	−23.1	−20.6
HCN···Ag_3	−10.3	−10.6

[a] The basis sets used to compute counterpoise corrected energies (kcal/mol) can be found in the text. We do not report the B3LYP energy for HCN−Ag due to density functional theory's poor performance with weakly bound systems.

The very different bonding natures of HCN−Ag and HCN−Cu are also reflected in the experimental data. The vibrational red shift and experimental dipole moment for HCN−Ag were found to be relatively small, especially when compared to the HCN−Cu complex. The small vibrational red shift of the C−H stretch alone can be misleading, as it will be discussed below, but taken together with the relatively small dipole moment, the experimental data strongly support the theoretical conclusions regarding a fundamental difference between the bonding nature of HCN−Ag and HCN−Cu. To begin with, the HCN−Cu dipole moment was measured to be very large (6.40 D), due to the significant charge transfer from the nitrogen lone pair to the singly occupied 4s orbital. This charge transfer was calculated to only be possible when the bond lengths between the nitrogen end of the HCN and the Cu atom were relatively short (<2 Å). Conversely, the HCN−Ag complex was measured here to have a smaller dipole moment (4.65 D) and is more consistent with the dipole moment being due to a dipole-induced polarization of the Ag atom. The vibrational red shifts will be discussed along with the higher order clusters further below.

The experimentally determined linear structure of HCN−Ag_2 is supported by both the MP2 and the DFT calculations. Considering that silver and copper share the same column on the periodic table, it is not surprising that a linear structure was also found for the HCN−Cu_2 complex. However, there are some differences, with the most obvious being the much larger metal−nitrogen bond length calculated for the HCN−Ag_2 cluster. The MP2 N−Ag bond distance reported in Figure 2B is 2.403 Å, while the corresponding MP2 bond length for HCN−Cu_2 was found to be a much shorter (1.838 Å). The binding energy between the HCN and the Ag_2 reflects this larger bond length and is substantially smaller than the HCN−Cu_2 binding energy (Table 6). It is interesting to note, however, that we still observe a very large jump in binding energy when moving from the HCN−Ag binary system to the HCN−Ag_2, similar to what was calculated for the HCN−Cu_n system. Table 6 presents the calculated binding energy data for both systems.

As it was discussed in an earlier theoretical publication on the properties of Cu_n−CO clusters, which also calculated a large increase in binding energy, the Cu_2 complex has the ability to reduce Pauli repulsion between the carbon and the Cu by polarizing electron density into its (4s − 4s) σ^* molecular orbital. This density deformation allows the CO and Cu_2 dimer to approach more closely and have an increased interaction. The exact same mechanism was observed in the electron density

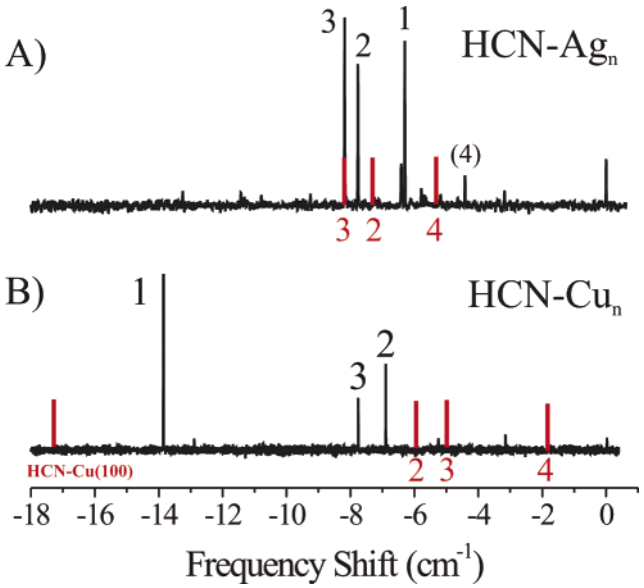

Figure 10. Direct comparison of the (A) HCN−Ag_n and (B) HCN−Cu_n pendular spectra. The red markers correspond to the B3LYP harmonic frequency shifts of each monoligated complex. The experimental frequency shift for HCN on a Cu(100) surface is also shown.

difference plot of the HCN−Cu_2 complex (9B). Here, we subject the HCN−Ag_2 complex to the same electron density difference analysis to help visualize the flow of electrons in the HCN and Ag_2 subunits as they are brought together. The plot is given in Figure 9A and shows a similar qualitative picture of what was observed for the HCN−Cu_2 complex. (It should be noted that the contours used in the electron density difference plots given in Figure 9 are not equal for the HCN−Ag_n and HCN−Cu_n. The lower cutoff contours and smaller contour step sizes were used with the HCN−Ag_n data to reveal the qualitative similarities between it and the HCN−Cu_n data.) First, one can see that there is an increase in electron density in the (5s − 5s) σ^*, which is polarized away from the N−Ag bond. Second, there is a small increase in electron density between the N−Ag nuclei and is interpreted as a consequence of σ donation of the nitrogen's lone pair into the Ag_2 lowest unoccupied molecular orbital.

The doublet ground state of the HCN−Ag_3 cluster, shown in Figure 2, is a C_{2V} structure, matching the structure calculated and experimentally observed for HCN−Cu_3. Again, there is a large rise in binding energy when going from the HCN−Ag_2 to the HCN−Ag_3, which is investigated by calculating the electron density difference plots. Figure 9C shows the plot of HCN−Ag_3. Not only is there an increase in the electron density between the bond formed between the N and the Ag atoms, but there is also an increase in the density protruding out from the Ag atom. The latter is interpreted as the formation of π interaction between the p-derived orbitals on the Ag_3 cluster to the π antibonding orbitals on the HCN molecule. This is exactly the same σ donation and π backbonding pattern observed for the HCN−Cu_3 complex, albeit to a much lesser extent, which is reflected in the smaller binding energy.

Finally, let us end the discussion with the examination of the overall vibrational shifts of the HCN−Ag_n clusters. The pendular spectra of both the HCN−Ag_n and the HCN−Cu_n systems are given in Figure 8A,B, respectively. One of the most interesting aspects of the HCN−Cu_n study was the pattern exhibited by the C−H vibrational frequency shifts of single HCN molecule bound to the various Cu cluster sizes.[27] The data were augmented by prior IR data of HCN on a Cu(100) surface, which provided a bulk limit on which to compare our results.[69] The previous data are summarized in Figure 10B, where the HCN−Cu C−H stretch is nearest to the bulk value and the HCN−Cu_n ($n = 2-3$) complexes are blue-shifted with respect to the HCN−Cu(100) value. In an attempt to follow the trend beyond the experimentally observed complexes, we calculated the structure and vibrational shift of the HCN−Cu_4 complex, which was found to be further shifted to the blue of the bulk HCN−Cu(100) shift. Obviously, the Cu cluster size must reach a size where the vibrational shifts "turn around" and begin to move back toward the bulk value. We postulated that this point will be reached when the cluster size is such that the radius of curvature of the cluster begins to approximate a flat surface. Unfortunately, we are unaware of IR studies of HCN on bulk Ag surfaces, but as one can see in Figure 10A, the vibrational shifts of the HCN−Ag_n complexes (excluding the binary systems) exhibit a qualitatively similar pattern to the HCN−Cu_n spectrum. The $n = 2$ and $n = 3$ species are found relatively close to one another while the $n = 4$ complex is blue-shifted with respect to the smaller complexes. The overall magnitude of the shifts in the HCN−Ag_n data is smaller than HCN−Cu_n, which seems to suggest that the pattern is dictated by the binding energy between the HCN and the metal cluster (Table 6), rather than the polarizabilites of the metal atoms themselves. For example, if the shifts were due primarily to van der Waals type dipole-induced dipole interactions alone, one would expect the larger, more polarizable Ag atoms (7.9 Å^3)[70] to have larger shifts than the Cu (6.7 Å^3)[70]-containing complexes. The correlation between experimental vibrational shifts and binding energy could be investigated more thoroughly using an adsorbate, such as CO, that has vibrational shifts that are more sensitive to small changes in bonding nature. Such experiments will undoubtedly take place as technological advances in high-resolution mid-IR lasers progress.

V. Summary

Here, we have reported the high-resolution IR spectra of the C−H stretch in HCN−Ag_n ($n = 1-3$) embedded in helium nanodroplets. Stark spectra are also given for each complex, thus giving experimental dipole moments. The symmetry of the spectra combined with the ab initio calculations provided a means to assign the structures of the observed clusters. The HCN−Ag binary complex has a vibrationally averaged linear structure. The HCN−Ag_2 is also linear, while the HCN−Ag_3 complex takes on a C_2 V geometry. All HCN ligands are bound to their Ag counterparts through the nitrogen. We also tentatively assigned the pendular band of HCN−Ag_4 based upon pick-up cell conditions and DFT vibrational calculations.

The spectra, vibrational shifts, and theoretical data were compared to that of the HCN−Cu_n system. The HCN−Ag binary complex was determined to be fundamentally different from the HCN−Cu complex. The calculated binding energy between the nitrogen end of HCN and the metal atom was much smaller in the HCN−Ag case, consistent with the smaller experimental vibrational shift and dipole moment. The higher order clusters, although smaller in magnitude, were found to repeat the trend in binding energies that was found in the HCN−Cu_n system. It was also found through electron density difference plots that the nature of binding was essentially the same for both the HCN−Ag_n ($n = 2-3$) and the HCN−Cu_n ($n = 2-3$).

Acknowledgment. This work was supported by the NSF (CHE-04-46594). Many thanks to Gary Douberly and Rebecca Wolfe for their critical readings of this manuscript.

References and Notes

(1) Duncan, M. A., Ed. *Advances in Metal and Semiconductor Clusters*; JAI Press: Greenwich, 1993.

(2) Knickelbein, M. B. *Annu. Rev. Phys. Chem.* **1999**, *50*, 79−115.

(3) Moskovits, M., Ed. *Metal Clusters*; Wiley-Interscience: New York, 1986.

(4) Klabunde, K. J. *Free Atoms, Clusters and Nanoscale Particles*; Academic Press: New York, 1994.

(5) Duncan, M. A. *Int. Rev. Phys. Chem.* **2003**, *22*, 407−435.

(6) Boese, A. D.; Schneider, H.; Gloss, A. N.; Weber, J. M. *J. Chem. Phys.* **2005**, *122*, 154301.

(7) Haruta, M.; Tsubota, S.; Kobayashi, T.; Kageyama, H.; Genet, M. J.; Delmon, B. *J. Catal.* **1993**, *144*, 175−192.

(8) Sanchez, A.; Abbet, S.; Heiz, U.; Schneider, W. D.; Hakkinen, H.; Barnett, R. N.; Landman, U. J. *Phys. Chem. A* **1999**, *103*, 9573−9578.

(9) Naydenov, B.; Ryan, P.; Teague, L. C.; Boland, J. *J. Phys. Rev. Lett.* **2006**, *97*, 098304.

(10) Yoder, N. L.; Guisinger, N. P.; Hersam, M. C.; Jorn, R.; Kaun, C. C.; Seideman, T. *Phys. Rev. Lett.* **2006**, *97*, 187601.

(11) Bernhardt, T. M. *Int. J. Mass Spectrom.* **2005**, *243*, 1−29.

(12) Weis, P.; Welz, O.; Vollmer, E.; Kappes, M. M. *J. Chem. Phys.* **2004**, *120*, 677−684.

(13) Rabin, I.; Schulze, W.; Ertl, G. *Chem. Phys. Lett.* **1999**, *312*, 394−398.

(14) Evans, C.; Gerry, M. C. L. *J. Phys. Chem. A* **2001**, *105*, 9659−9663.

(15) Koretsky, G. M.; Knickelbein, M. B. *J. Chem. Phys.* **1997**, *107*, 10555−10566.

(16) Fielicke, A.; Rabin, I.; Meijer, G. *J. Phys. Chem. A* **2006**, *110*, 8060−8063.

(17) Knickelbein, M. B.; Koretsky, G. M. *J. Phys. Chem. A* **1998**, *102*, 580−586.

(18) Koretsky, G. M.; Knickelbein, M. B.; Rousseau, R.; Marx, D. *J. Phys. Chem. A* **2001**, *105*, 11197−11203.

(19) Choi, M. Y.; Miller, R. E. *Phys. Chem. Chem. Phys.* **2005**, *7*, 3565−3573.

(20) Merritt, J. M.; Kupper, J.; Miller, R. E. *Phys. Chem. Chem. Phys.* **2005**, *7*, 67−78.

(21) Douberly, G. E.; Merritt, J. M.; Miller, R. E. *Phys. Chem. Chem. Phys.* **2005**, *7*, 463−468.

(22) Nauta, K.; Moore, D. T.; Stiles, P. L.; Miller, R. E. *Science* **2001**, *292*, 481−484.

(23) Schmied, R.; Carcabal, P.; Dokter, A. M.; Lonij, V. P. A.; Lehmann, K. K.; Scoles, G. *J. Chem. Phys.* **2004**, *121*, 2701−2710.

(24) Stienkemeier, F.; Higgins, J.; Callegari, C.; Kanorsky, S. I.; Ernst, W. E.; Scoles, G. *Z. Phys. D* **1996**, *38*, 253−263.

(25) Diederich, T.; Tiggesbaumker, J.; Meiwes-Broer, K. H. *J. Chem. Phys.* **2002**, *116*, 3263−3269.

(26) Diederich, T.; Doppner, T.; Braune, J.; Tiggesbaumker, J.; Meiwes-Broer, K. H. *Phys. Rev. Lett.* **2001**, *86*, 4807−4810.

(27) Stiles, P. L.; Miller, R. E. *J. Phys. Chem. A* **2006**, *110*, 10225−10235.

(28) Stiles, P. L.; Moore, D. T.; Miller, R. E. *J. Chem. Phys.* **2004**, *121*, 3130.

(29) Stiles, P. L.; Miller, R. E. *J. Phys. Chem. A* **2006**, *110*, 5620−5628.

(30) Fournier, R. *J. Chem. Phys.* **1995**, *102*, 5396−5407.

(31) Designed and constructed by G. E. Douberly.

(32) Nauta, K.; Moore, D. T.; Miller, R. E. *Faraday Discuss. Chem. Soc.* **1999**, *113*, 261−278.

(33) Nauta, K.; Miller, R. E. *J. Chem. Phys.* **1999**, *111*, 3426−3433.

(34) Lewerenz, M.; Schilling, B.; Toennies, J. P. *Chem. Phys. Lett.* **1993**, *206*, 381−387.

(35) Lewerenz, M.; Schilling, B.; Toennies, J. P. *J. Chem. Phys.* **1995**, *102*, 8191−8207.

(36) Huang, Z. S.; Jucks, K. W.; Miller, R. E. *J. Chem. Phys.* **1986**, *85*, 3338−3341.

(37) Rost, J. M.; Griffin, J. C.; Friedrich, B.; Herschbach, D. R. *Phys. Rev. Lett.* **1992**, *68*, 1299−1301.

(38) Block, P. A.; Bohac, E. J.; Miller, R. E. *Phys. Rev. Lett.* **1992**, *68*, 1303−1306.

(39) Nauta, K.; Miller, R. E. *Phys. Rev. Lett.* **1999**, *82*, 4480−4483.

(40) Stiles, P. L.; Nauta, K.; Miller, R. E. *Phys. Rev. Lett.* **2003**, *90*, 135301.

(41) Werner, H. J.; Knowles, P. J.; Amos, R. D.; Bernhardsson, A.; Berning, A.; Celani, P.; Cooper, D. L.; Deegan, M. J. O.; Dobbyn, A. J.; Eckert, F.; et al. *Molpro*; University College Cardiff Consultants Limited: Wales, United Kingdom, 2002.

(42) Frisch, M. J.; Trucks, G. W.; Schlegel, H. B.; Scuseria, G. E.; Robb, M. A.; Cheeseman, J. R.; Montgomery, J. A., Jr.; Vreven, T.; Kudin, K. N.; Burant, J. C.; Millam, J. M.; Iyengar, S. S.; Tomasi, J.; Barone, V.; Mennucci, B.; Cossi, M.; Scalmani, G.; Rega, N.; Petersson, G. A.; Nakatsuji, H.; Hada, M.; Ehara, M.; Toyota, K.; Fukuda, R.; Hasegawa, J.; Ishida, M.; Nakajima, T.; Honda, Y.; Kitao, O.; Nakai, H.; Klene, M.; Li, X.; Knox, J. E.; Hratchian, H. P.; Cross, J. B.; Bakken, V.; Adamo, C.; Jaramillo, J.; Gomperts, R.; Stratmann, R. E.; Yazyev, O.; Austin, A. J.; Cammi, R.; Pomelli, C.; Ochterski, J. W.; Ayala, P. Y.; Morokuma, K.; Voth, G. A.; Salvador, P.; Dannenberg, J. J.; Zakrzewski, V. G.; Dapprich, S.; Daniels, A. D.; Strain, M. C.; Farkas, O.; Malick, D. K.; Rabuck, A. D.; Raghavachari, K.; Foresman, J. B.; Ortiz, J. V.; Cui, Q.; Baboul, A. G.; Clifford, S.; Cioslowski, J.; Stefanov, B. B.; Liu, G.; Liashenko, A.; Piskorz, P.; Komaromi, I.; Martin, R. L.; Fox, D. J.; Keith, T.; Al-Laham, M. A.; Peng, C. Y.; Nanayakkara, A.; Challacombe, M.; Gill, P. M. W.; Johnson, B.; Chen, W.; Wong, M. W.; Gonzalez, C.; Pople, J. A. *Gaussian 03*, revision C.02; Gaussian, Inc.: Wallingford, CT, 2004.

(43) Dolg, M.; Wedig, U.; Stoll, H.; Preuss, H. *J. Chem. Phys.* **1987**, *86*, 866−872.

(44) Martin, J. M. L.; Sundermann, A. *J. Chem. Phys.* **2001**, *114*, 3408−3420.

(45) Dkhissi, A.; Alikhani, M. E.; Bouteiller, Y. *J. Mol. Struct.* **1997**, *416*, 1−9.

(46) Morse, M. D. *Chem. Rev.* **1986**, *86*, 1049−1109.

(47) Wang, X. W.; Wan, X. W.; Zhou, H.; Takami, S.; Kubo, M.; Miyamoto, A. *J. Mol. Struct. (THEOCHEM)* **2002**, *579*, 221−227.

(48) Yoon, J.; Kim, K. S.; Baeck, K. K. *J. Chem. Phys.* **2000**, *112*, 9335−9342.

(49) Zhou, J.; Li, Z.; Wang, W.; Fan, K. *J. Phys. Chem. A* **2006**, *110*, 7167−7172.

(50) Joshi, A. M.; Tucker, M. H.; Delgass, W. N.; Thomson, K. T. *J. Chem. Phys.* **2006**, *125*, 194707.

(51) Poater, A.; Duran, M.; Jaque, P.; Toro-Labbe, A.; Sola, M. *J. Phys. Chem. B* **2006**, *110*, 6526−6536.

(52) Cao, Z.; Wang, Y.; Zhu, J.; Wu, W.; Zhang, W. *J. Phys. Chem. B* **2002**, *106*, 9649−9654.

(53) Friedrich, B.; Herschbach, D. R. *Nature* **1991**, *353*, 412−414.

(54) Abbate, A. D.; Kawai, T.; Moore, C. B.; Chin, C. T. *Surf. Sci.* **1984**, *136*, L19−L24.

(55) Cheng, C.; Ho, P.; Moore, C. B.; Zughul, M. B. *J. Phys. Chem.* **1984**, *88*, 296−300.

(56) Moore, C. B.; Weisshaar, J. C. *Annu. Rev. Phys. Chem.* **1983**, *34*, 525−555.

(57) Kwon, Y.; Ceperley, D. M.; Whaley, K. B. *J. Chem. Phys.* **1996**, *104*, 2341−2348.

(58) Kwon, Y.; Whaley, K. B. *J. Chem. Phys.* **2003**, *119*, 1986−1995.

(59) Kwon, Y.; Whaley, K. B. *Phys. Rev. Lett.* **1999**, *83*, 4108−4111.

(60) Draeger, E. W.; Ceperley, D. M. *Phys. Rev. Lett.* **2003**, *90*, 065301.

(61) Lehmann, K. K.; Callegari, C. *J. Chem. Phys.* **2002**, *117*, 1595−1603.

(62) Callegari, C.; Conjusteau, A.; Reinhard, I.; Lehmann, K. K.; Scoles, G.; Dalfovo, F. *Phys. Rev. Lett.* **1999**, *83*, 5058−5061.

(63) Moore, D. T.; Oudejans, L.; Miller, R. E. *J. Chem. Phys.* **1999**, *110*, 197−208.

(64) Douberly, G. E.; Miller, R. E. *J. Phys. Chem. A* **2007**, *111*, 7292−7302.

(65) Douberly, G. E.; Stiles, P. L.; Miller, R. E. **2007**, submitted to press.

(66) Douberly, G. E.; Nauta, B. K.; Miller, R. E. *Chem. Phys. Lett.* **2003**, *377*, 384−390.

(67) Nauta, K.; Miller, R. E. *Chem. Phys. Lett.* **2001**, *346*, 129−134.

(68) Stiles, P. L.; Moore, D. T.; Miller, R. E. *J. Chem. Phys.* **2003**, *118*, 7873−7881.

(69) Celio, H.; Mills, P.; Jentz, D.; Pae, Y. I.; Trenary, M. *Langmuir* **1998**, *14*, 1379−1383.

(70) Lide, D. R., Ed. *CRC Handbook of Chemistry and Physics*; CRC Press: Boca Raton, 1990; Vol. 71.